Controlled coherent-coupling and dynamics of exciton complexes in a $MoSe_2$ monolayer

2D Materials

OPEN ACCESS

RECEIVED
8 January 2023

REVISED
28 February 2023

ACCEPTED FOR PUBLICATION
20 March 2023

PUBLISHED
3 April 2023

PAPER

Controlled coherent-coupling and dynamics of exciton complexes in a $MoSe_2$ monolayer

Aleksander Rodek[1,*], Thilo Hahn[2], James Howarth[3], Takashi Taniguchi[4], Kenji Watanabe[5], Marek Potemski[1,6,7], Piotr Kossacki[1,*], Daniel Wigger[8] and Jacek Kasprzak[1,9,10,*]

[1] Faculty of Physics, University of Warsaw, ul. Pasteura 5, 02-093 Warszawa, Poland
[2] Institute of Solid State Theory, University of Münster, 48149 Münster, Germany
[3] National Graphene Institute, University of Manchester, Booth St E, Manchester, M13 9PL, United Kingdom
[4] International Center for Materials Nanoarchitectonics, National Institute for Materials Science, 1-1 Namiki, Tsukuba 305-0044, Japan
[5] Research Center for Functional Materials, National Institute for Materials Science, 1-1 Namiki, Tsukuba 305-0044, Japan
[6] Laboratoire National des Champs Magnétiques Intenses, CNRS-UGA-UPS-INSA-EMFL, 25 Av. des Martyrs, 38042 Grenoble, France
[7] CENTERA Labs, Institute of High Pressure Physics, PAS, 01-142 Warsaw, Poland
[8] School of Physics, Trinity College Dublin, Dublin 2, Ireland
[9] Univ. Grenoble Alpes, CNRS, Grenoble INP, Institut Néel, 38000 Grenoble, France
[10] Walter Schottky Institut and TUM School of Natural Sciences, Technische Universität München, 85748 Garching, Germany
[*] Authors to whom any correspondence should be addressed.

E-mail: aleksander.rodek@fuw.edu.pl, piotr.kossacki@fuw.edu.pl and jacek.kasprzak@neel.cnrs.fr

Keywords: transition metal dichalcogenides, coherent nonlinear spectroscopy, ultrafast exciton dynamics, coherent coupling, two-dimensional spectroscopy, four-wave mixing, optical microscopy and imaging

Supplementary material for this article is available online

Abstract

Quantifying and controlling the coherent dynamics and couplings of optically active excitations in solids is of paramount importance in fundamental research in condensed matter optics and for their prospective optoelectronic applications in quantum technologies. Here, we perform ultrafast coherent nonlinear spectroscopy of a charge-tunable $MoSe_2$ monolayer. The experiments show that the homogeneous and inhomogeneous line width and the population decay of exciton complexes hosted by this material can be directly tuned by an applied gate bias, which governs the Fermi level and therefore the free carrier density. By performing two-dimensional spectroscopy, we also show that the same bias-tuning approach permits us to control the coherent coupling strength between charged and neutral exciton complexes.

1. Introduction

The ability to isolate monolayer flakes of semiconducting transition-metal dichalcogenides (TMDs), such as $MoSe_2$, and the discovery of their enhanced light–matter interaction at the monolayer limit a decade ago [1, 2] established a novel benchmark for semiconductor optics. The combination of heavy effective masses and spin-valley locking—both inherent in the monolayer's band structure—with a large out-of-plane dielectric contrast result in particularly strong Coulomb interactions among free carriers hosted by TMD monolayers [3, 4]. For the same reason, the exciton transitions display a non-hydrogenic excitation spectrum [5] and have large binding energies and oscillator strengths [6, 7], such that they dominate the optical response of TMD materials even at room temperature.

Further to that, the ability to stack different sorts of layered van der Waals materials, such as TMDs, hexagonal boron nitride (hBN), graphene or graphite, into van der Waals heterostructures [8, 9], facilitates the fabrication of optoelectronic devices [10–14]. Sandwiching layered TMDs or other materials between high quality hBN diminishes the electronic disorder and protects them from degradation by ambient agents. In general, the hBN-encapsulation procedure reduces the exciton's spectral inhomogeneous broadening $\hbar\sigma$, thus improving the optical performance of TMDs [15–18]. It even enables reaching the homogeneous limit for the exciton's spectral line shape [19, 20]. This has been a milestone for

monolayer spectroscopy, as it enhances the visibility of phenomena previously blurred by different types of inhomogeneity, with the appearance of a novel destructive photon echo being an example [21].

We are employing a four-wave mixing (FWM) spectroscopy approach to study the coherent optical properties of TMD exciton complexes. This method is recently gaining more popularity for the investigation of layered semiconductors: Besides the fundamental studies of the exciton coherence and population dynamics in different TMD systems [19, 22, 23] it was also used to probe intervalley scattering processes [24], valley coherence times [25], and mechanisms of exciton broadening [26]. In particular it allowed for first observations of biexcitons [27, 28] or coupling between different exciton states [28] in various TMD materials.

Electron beam lithography and metal deposition can further be employed to complement van der Waals heterostructures with electronic contacts and gates [29, 30]. In this way, one can inject carriers into TMD monolayers, permitting us to control the free electron density n_e in our sample. This is crucial, not only for optoelectronic applications, but also when exploring the fundamental physics of correlated many-body systems in solids; landmark examples being the recent revelation of Wigner crystals in a gate-tunable $MoSe_2$ monolayer [31] or optical sensing of the quantum Hall effect in graphene [32].

The presence of free carriers modifies the excitonic optical response substantially [33, 34], similarly as was shown and partially explained for semiconductor quantum wells [35–38]. Firstly, it is supposed that free carriers affect the relative absorption (oscillator or effective dipole strength) and the possible couplings between neutral excitons (X) and (negatively) charged excitons (X^-), also called trions. Secondly, the exciton's dephasing and therefore the spectral line shape should be sensitive to the electron density n_e [39], in an analogous way as it depends on the total exciton density, through the mechanisms called excitation induced dephasing [20, 40, 41], sometimes described by a local field effect [42, 43]. Thirdly, with increasing n_e the exciton complexes are screened more efficiently from intrinsic disorder, which in turn should reduce their inhomogeneous broadening [3, 44], further impacting the excitons' radiative decay rates [45]. Here, we address the basic interplay between free carriers n_e, excitons X, and trions X^- by performing coherent nonlinear spectroscopy [46, 47] of a gated and hBN-encapsulated $MoSe_2$ monolayer.

2. Sample and experiment

A microscopy image of our device is presented in figure 1(a), where the $MoSe_2$ monolayer flake (marked in red) is encapsulated between thin bottom (dashed white) and top (solid white) hBN films. The bottom graphite flake (dashed black) lies under the hBN spacer, while the top few-layer graphene flakes (solid black) are adjacent to the $MoSe_2$ as shown in the layer schematic in the top right inset. The graphite and graphene operate as bottom and top gates, respectively. Details regarding the fabrication of our device are provided in the supporting information (SI). We have fabricated and investigated two samples of the same design, which show very similar results throughout the studied properties.

The device permits us to control the free electron density n_e by applying a gate bias U via the gold bands, as shown in yellow in figure 1(a), connecting with both graphite and graphene layers acting as electrodes. When increasing the bias and therefore n_e we observe modifications of the optical response of the monolayer, both in the transition energy and the spectral line shapes, as shown in the white-light reflection contrast spectra presented in figure 1(b). We note that by varying n_e we can alter the relative spectral intensities of X and X^-, as quantified in (c). We see that already the linear optical response, as observed in reflectance, is tuned when increasing n_e, as the oscillator strength shifts from X to X^-—we will come back to this point in the last section.

To infer the coherent nonlinear response of excitons, we perform FWM microscopy, similarly as in our recent works [22]. We use three, co-linearly polarized pulses of 150 femtosecond duration, here labeled as $\mathcal{E}_{1,2,3}$, that can be tuned into resonance with the excitonic transitions. The beams are focused down to a diffraction-limited spot on the sample's surface, placed in a helium flow cryostat, setting the temperature at $T = 8$ K for all experiments. The complex-valued FWM signal, generated in a standard, so-called photon echo, configuration is retrieved in reflectance by combining optical heterodyning and spectral interferometry with a reference pulse [48]. The reference beam is focused through the same objective (NA = 0.65) below $\mathcal{E}_{1,2,3}$ and is reflected from the neighboring hBN without $MoSe_2$, as shown in figure 1(a) by the white dots.

To investigate the exciton's coherence dynamics we measure the FWM amplitude as a function of time delay τ_{12} between the first and the second arriving pulses, while fixing τ_{23}. Conversely, the exciton's population dynamics is probed in FWM when varying the delay τ_{23}, while fixing τ_{12}. These pulse sequences are depicted in figures 2(a) and 3(a), respectively. We note that for all experiments we keep the same excitation conditions of 0.3 μW average power for each of the beams, generating an exciton density of a few 10^{10} cm^{-2} [20, 22]. To confirm the expected linear scalings of the FWM amplitude with the pulse areas of $\mathcal{E}_{1,2,3}$ for small powers, we checked the FWM power dependence (see SI figure S1), also monitoring that the excitation induced dephasing can be neglected for this range of exciton densities [20].

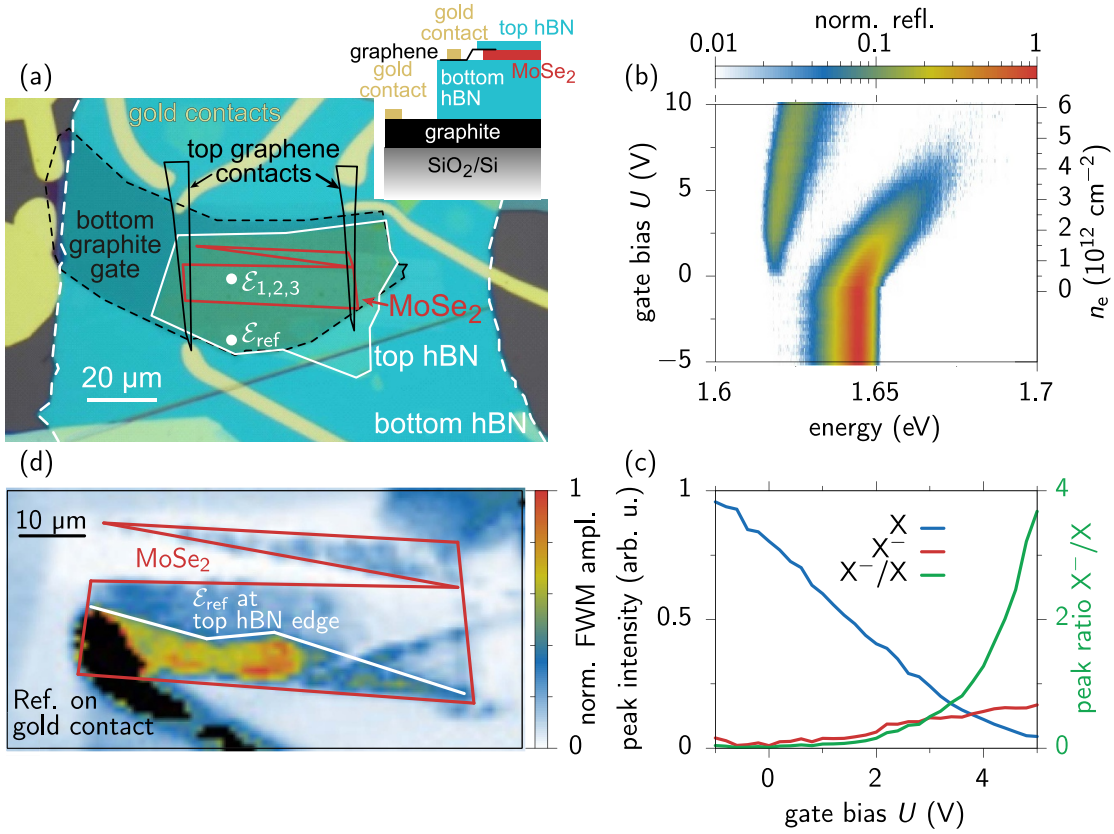

Figure 1. Investigated $MoSe_2$ device and optical characterization. (a) Optical image of the heterostructure. The individual components are marked by colored lines and the white dots mark the positions of the laser beams for the FWM measurements and the inset shows the layer structure of the sample. (b) Reflectance contrast spectrum of the sample as a function of the applied voltage showing the neutral (X) and negatively-charged (X^-) exciton transitions. (c) Individual peak intensities X in blue and X^- in red from (b) and their ratio in green. (d) Imaging of the time-integrated FWM at $\tau_{12} = 1.2$ ps. The black area in the lower-left corner of the image is an experimental artefact generated when the reference beam impinges on the highly reflecting metallic contact ~10 μm below the edge of the $MoSe_2$ monolayer. The outline of the $MoSe_2$ flake is marked in red and the line where the reference beam $\mathcal{E}_{ref}$ crosses the bottom edge of the top hBN flake in white.

To characterize the overall device, we set $U = -0.5$ V and perform a FWM amplitude mapping across the $MoSe_2$ flake for $\tau_{12} = 1.2$ ps, by scanning the objective's position. The resulting time-integrated FWM image is presented in figure 1(d) (for detailed analysis of this imaging see SI figures S2–S4). The dominant signals reflect the third-order optical susceptibility of the $MoSe_2$ monolayer (red line). Note, that the generated FWM is weaker in the upper part of the flake, which is due to the reduced reflectance of the reference pulse $\mathcal{E}_{ref}$ when impinging on the top hBN. This crossover between low and high FWM amplitude regions (marked in white) faithfully follows the shape of the top hBN's edge when $\mathcal{E}_{ref}$ leaves the top hBN, while the other pulses $\mathcal{E}_{1,2,3}$ still probe the fully encapsulated $MoSe_2$ monolayer.

In time-resolved FWM, a typical case presented in figure 2(b), without introducing free carriers we observe a more or less pronounced photon echo [22, 23, 26], which is a consequence of inhomogeneous broadening $\hbar\sigma$. The latter induces rephasing of the signal for $t = \tau_{12}$, such that normally the echo is aligned with the diagonal in the (t, τ_{12})-space, as depicted as dashed diagonal in (b). However, for short delays $\tau_{12} < 0.5$ ps we spot deviations from the typical echo. In this range the signal is retarded in time, such that the transient is not following the diagonal, and is instead curved, into a comet-like shape. The echo distortion is readily reproduced, when taking into account the local field effect [21], representing an effective exciton–exciton interaction, and is described in leading order in the local field coupling by

$$|p_{\mathrm{FWM}}(t,\tau_{12})| \sim \Theta(\tau_{12})\Theta(t)te^{-\beta(t+\tau_{12})-\frac{1}{2}\sigma^2(t-\tau_{12})^2} + \Theta(-\tau_{12})\Theta(t+\tau_{12})(t+\tau_{12}) \times e^{-\beta(t-\tau_{12})-\frac{1}{2}\sigma^2(t-\tau_{12})^2}. \quad (1)$$

The fitted (t, τ_{12})-dynamics is presented in figure 2(c), from which we extract homogeneous β and inhomogeneous σ dephasing rates and corresponding full-width at half-maxima

(FWHM) spectral broadenings $\hbar\beta = 0.86\,\mathrm{meV}$ and $2\sqrt{2\ln(2)}\hbar\sigma = \hbar\tilde{\sigma} = 3.9\,\mathrm{meV}$, respectively. By inspecting spectrally-resolved FWM mappings, we reveal typical fluctuations of the exciton's central energy ($\approx\pm5\,\mathrm{meV}$) and line widths ($\approx\pm1\,\mathrm{meV}$), as shown in figure S2 in the SI, attributed to varying strain generated during the sample assembly [49–51]. We therefore fix the excitation spot for the entire experiment, as marked in figure 1(a), to probe an area of relatively small σ within the distribution. The same mapping is performed for the time-resolved FWM signal, which allows to extract homogeneous and inhomogeneous broadenings, summarized in SI figure S3. We find an expected and pronounced correlation between σ and the FWHM of the FWM spectra, as shown in SI figure S4. There, we also find a correlation between the exciton transition energy and the inhomogeneous broadening.

3. Coherence dynamics of neutral and charged excitons

We now proceed to the investigation of the exciton homogeneous linewidth $\hbar\beta$ depending on the induced electron density n_e. For this purpose, we center the excitation at the exciton energy, which for the investigated area equals 1640 meV, and measure the photon echo as a function of the gate bias U. Exemplary exciton coherence dynamics, i.e. time-integrated FWM amplitudes as a function of τ_{12}, are shown in figure 2(d) (blue dots). Due to the local field, the measured dynamics deviate from simple combined exponential and Gaussian decays according to equation (1). The corresponding fits are shown as pale blue lines and reproduce the experiments well. The data clearly indicate a growth of the dephasing rate when increasing the electron density (top to bottom). All fitted homogeneous broadenings are presented in (f, blue filled circles) as function of the gate bias, which quantifies the impression of a strong rise of $\hbar\beta$ with increasing n_e. The fitted dynamics also yield $\hbar\tilde{\sigma}$ as a function of n_e (f, blue open circles). Note, that for the fits we used the entire signal dynamics in real and delay time from which we also extract the time-integrated data in figures 2(d) and (e). Interestingly, the inhomogeneous broadening is suppressed efficiently, when injecting more electrons. The FWM transient thus evolves from the photon echo to free-induction decay like, as we explicitly show in SI figure S5. This strikingly shows that the excitons become less sensitive to the underlying disorder, which can be static due to the strain or dynamic via fluctuating charges. With increasing n_e, the disorder thus gets screened more efficiently and the applied voltage can neutralize fluctuating charges [44], both mechanisms making the system less inhomogeneous. We have previously found that the reduced inhomogeneity goes hand-in-hand with a shortening of the excitons' radiative lifetime [19]. The small rise of the X's inhomogeneous broadening at $U > 4$ V is an artefact from the weak optical response which results in an increased uncertainty of the fit. This is also reflected by the significant increase of the error bars (shaded area).

The second resonance, occurring at 1620 meV is the charged exciton transition X^-, which we selectively address by centering the laser pulse spectrum to this energy. We carry out the same routine as before to determine the charged exciton's homogeneous and inhomogeneous broadening and their dependence on n_e. The results are presented in figures 2(e) and (f) in red colors. When comparing X's and X^-'s homogeneous broadenings in (f), we observe that for the same electron density the X broadening is significantly larger than that of X^-. This finding is similar to experiments performed on non-intentionally doped samples [25]. Following an intermediate drop with increasing n_e, we eventually also observe an increase of the charged exciton's homogeneous broadening accompanied by a decrease in inhomogeneous broadening (open red circles). The increased line width of both exciton complexes is attributed to the dephasing due to interactions with the Fermi-sea of electrons, similarly as in past studies on semiconductor quantum wells [39, 40].

With this, we evidence the control the inhomogeneous broadening and excitonic dephasings and thus the spectral line shape of the optical transitions, via a tunable gate bias introducing free carriers into the $MoSe_2$ monolayer. We distinguish this line broadening mechanism from the ones previously investigated in TMDs, i.e. phonon-induced [22, 23, 26, 49, 52] and excitation-induced dephasing [19, 20].

At this point, we remark that the measured behavior of dephasings does not match with a simple picture of the dipole (oscillator) strength transfer from X to X^- when increasing n_e. Assuming that the dephasing was entirely governed by the radiative lifetime, a reduction for the X (an increase for X^-) dipole strength should increase (reduce) the lifetime and consequently the dephasing time. However, the opposite trend is observed in figure 2(f). Next to the suppression of σ via screening, the second possible cause for this behavior is the presence of other decay channels that increase with a growing n_e, which would result in an accelerated dephasing while remaining close to a lifetime-limited condition. To shed light on the dominating decay mechanism, we thus measure FWM as a function of τ_{23}, monitoring the coherent population dynamics of X and X^-.

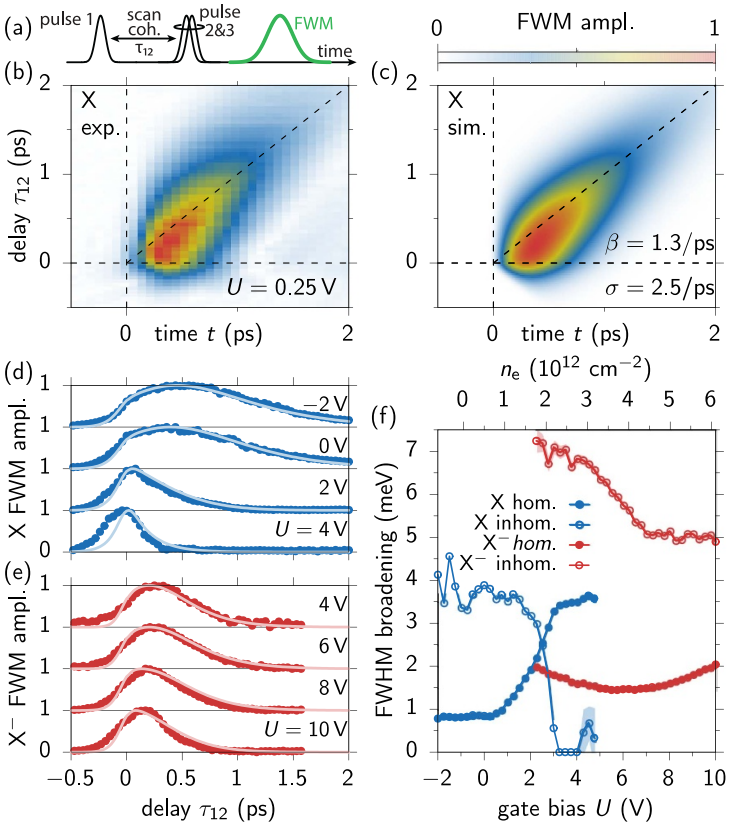

Figure 2. X and X$^-$ dephasing versus applied gate bias. (a) Scheme of the three-pulse FWM sequence probing coherence dynamics via τ_{12}. (b) Measured time-resolved FWM amplitude showing a clear photon echo. (c) Theoretical fit of (b) employing the local field model with the fitted homogeneous and inhomogeneous dephasing rates β and σ as given in the plot. (d) and (e) Exemplary time-integrated FWM amplitude dynamics as a function of τ_{12} for different gates biases. (d) For X and (e) for X$^-$. (f) Homogeneous (filled circles) and inhomogeneous (open circles) FWHM line widths extracted from (d), (e) and time-resolved data as a function of gates bias with X in blue and X$^-$ in red. The shaded areas show the uncertainties.

4. Population dynamics of neutral and charged excitons

In figure 3(b) we present the time-integrated FWM signals of X as a function of τ_{23} for selected gate biases (amplitude as red and phase as blue dots). As the FWM response is measured in a coherent fashion, we can retrieve its amplitude and phase, improving the insight into the involved decay processes affecting the excitonic populations that occur. A natural choice to describe this dependence is to consider a coherent superposition of several exponential decays [19, 53] via

$$\begin{aligned} S_{\mathrm{FWM}}(\tau_{23}, t) = A_{\mathrm{off}} \exp(i\varphi_{\mathrm{off}}) + \exp(i\varphi_{\mathrm{dr}} t) \\ \times \left\{ A_{\mathrm{nr}} \exp\left(i\varphi_{\mathrm{nr}} - \frac{\tau_{23}^2}{\tau_0^2} \right) \right. \\ + \sum_n A_n \left[1 + \mathrm{erf}\left(\frac{\tau_{23}}{\tau_0} - \frac{\tau_0}{2\tau_n} \right) \right] \\ \left. \times \exp\left(i\varphi_n + \frac{\tau_0^2}{2\tau_n^2} - \frac{\tau_{23}}{\tau_n} \right) \right\} \end{aligned} \quad (2)$$

where t is the measurement time of the FWM signal, $(A_{\mathrm{nr}}, \varphi_{\mathrm{nr}})$ are amplitude and phase of the two-photon absorption, (A_n, τ_n, φ_n) are the amplitude, characteristic time, and phase of a given decay processes, φ_{dr} is the phase drift during the measurement, $(A_{\mathrm{off}}, \varphi_{\mathrm{off}})$ are the amplitude and phase of the complex offset, and τ_0 is the pulse duration of the femto-second laser of around 150 fs.

As exemplarily represented by the fitted pale curves in figure 3(b, top), we find that for gate bias values $U \leqslant 0$, which corresponds to the charge-neutrality regime, i.e. no free electrons, the exciton's population dynamics can be fitted with a bi-exponential decay with characteristic timescales $\tau_1 < 1$ ps and $\tau_2 \approx 7$ ps. We plot the extracted timescales of the relaxation processes in figure 3(c). This result is in agreement with previous studies [22, 53], with the faster component being attributed to the exciton's decay, which can be due to several mechanisms: radiative recombination, non-radiative scattering into various momentum-dark states and localized states generated by the disorder, and finally X to X$^-$ conversion. The longer decay stems from the relaxation of thermalized higher k-vector exciton states, which scatter back into the light-cone (i.e. states with momentum values $|k| < n\omega/c$) through non-radiative processes and subsequently contribute to the FWM signal.

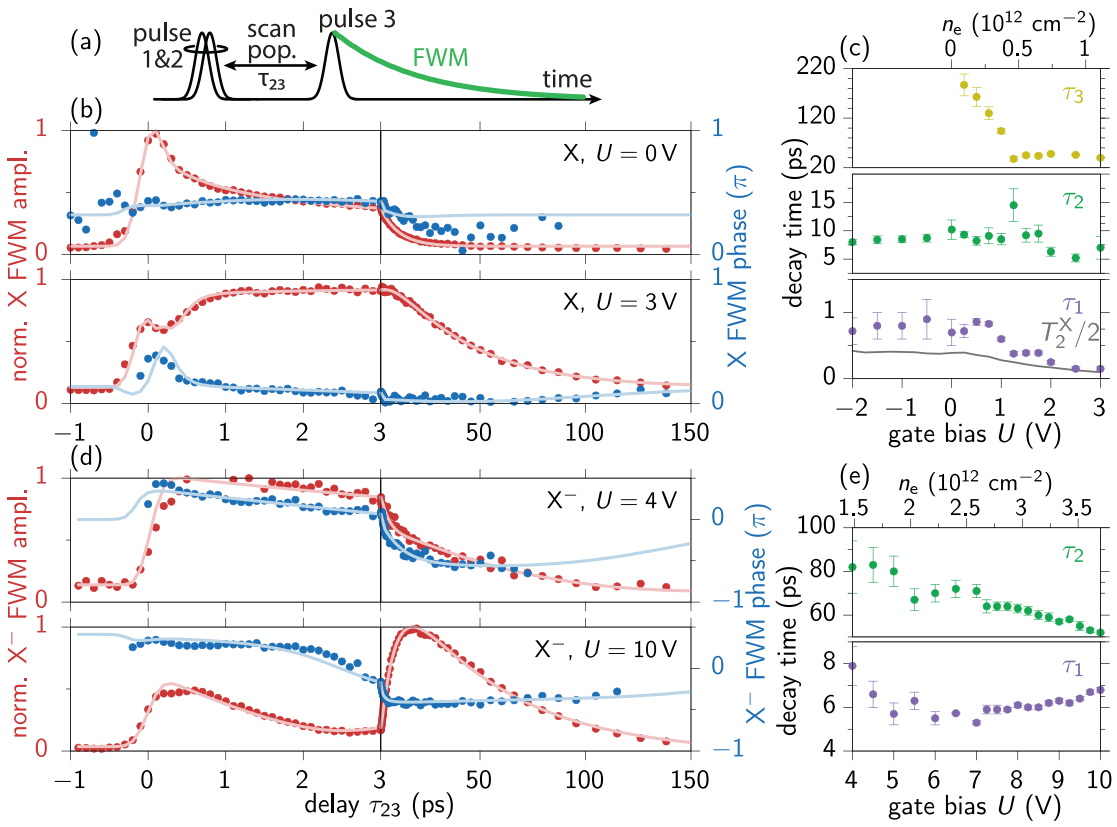

Figure 3. X and X$^-$ population dynamics versus gate bias. (a) Scheme of the three-pulse FWM probing the population dynamics. (b) Exemplary FWM amplitude (red dots) and phase (blue dots) dynamics of X as a function of τ_{23}, with fitted curves in pale colors, according to equation (1). (c) Extracted characteristic decay times of the three identified relaxation channels as a function of gate bias. The gray curve shows the blue data from figure 2(f) in the form $T_2^X = 1/\beta$. (d) and (e) same as (b) and (c) but for X$^-$.

With increasing gate bias U and thus n_e, the description of the observed population dynamics requires the introduction of a third, slower relaxation process τ_3. Earlier FWM experiments on samples naturally doped with electrons also indicate the presence of this long-lived component and attribute it to a decaying population of excitons with spin-forbidden transitions [53]. As the disorder is screened more efficiently with increasing n_e, we tentatively suggest that the observed faster dynamics could be also due to a weaker exciton localization.

The most pronounced change in the population dynamics, caused by the increase of n_e, can be observed during the first few picoseconds in figure 3(a). For positive U in figure 3(c), we observe a rapid increase of the fastest relaxation rate. This behavior, fortified by the shift of the FWM phase, occurs in the same voltage range as the previously mentioned shortening of the exciton dephasing time (see blue dots in figure 2(f)). Interestingly, when comparing the retrieved τ_1 values with $T_2^X/2 = 1/(2\beta)$ (gray line in figure 3(c, bottom)), we see the same trend with increasing bias. In particular, we find that for large gate biases the measurements approach $\tau_1 = T_2^X/2$ for $U \approx 3$ V and therefore the special situation of lifetime-limited dephasing. This result is also in line with the previous finding that the exciton loses nearly all inhomogeneous broadening for $U > 3$ V and therefore the dominant dephasing mechanism for smaller U.

In figures 3(d) and (e) we present analogous data from the measurements where the excitation energy is tuned to the charged exciton transition X$^-$. In this case, we only observe two distinct relaxation processes [53, 54] contributing to the investigated range of τ_{23}. X$^-$ is the lowest energy state and—in contrast to X—cannot relax to other excitonic states. Consequently, the initial decay of X$^-$ of around 6 ps, reflects its radiative and non-radiative recombination. We note here also, that the simple extension of the light-cone escape process as for the neutral excitons is now not valid for X$^-$. The free carrier leftover after the recombination allows for the additional momentum transfer and recombination of X$^-$ from non-zero k-vectors [55, 56].

5. Controlled coherent coupling between neutral and charged excitons

So far, we have investigated the coherence dynamics of X and X$^-$ separately, by selectively addressing the respective resonances. Conversely, when the two complexes are excited simultaneously, both exciton species coexist and interact with each other. To trigger

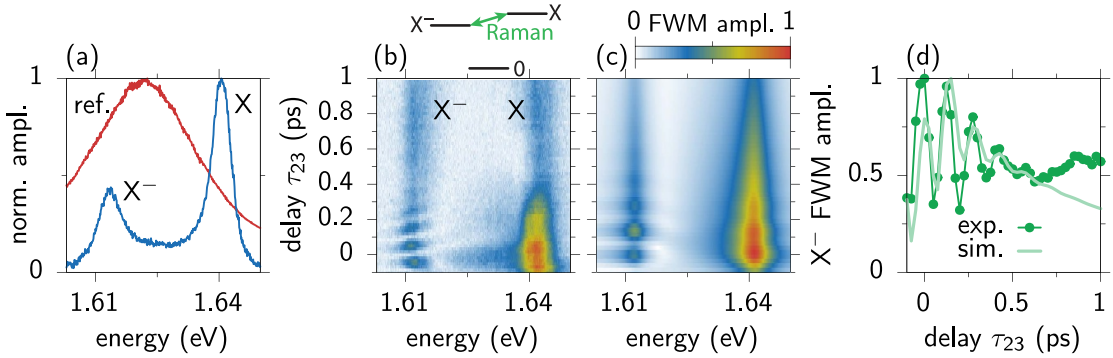

Figure 4. Quantum beat of the X–X$^-$ Raman coherence revealed in the population dynamics. (a) Amplitude of the FWM spectra of X and X$^-$ in blue together with the amplitude of reference spectrum in red. (b) Spectral dynamics of the FWM amplitude as a function of τ_{23} showing a clear beating of X$^-$. (c) Theoretical simulation of (b). (d) Dynamics of the X$^-$ single after spectral integration over the respective peak. Experiment as green dots and simulation as pale line.

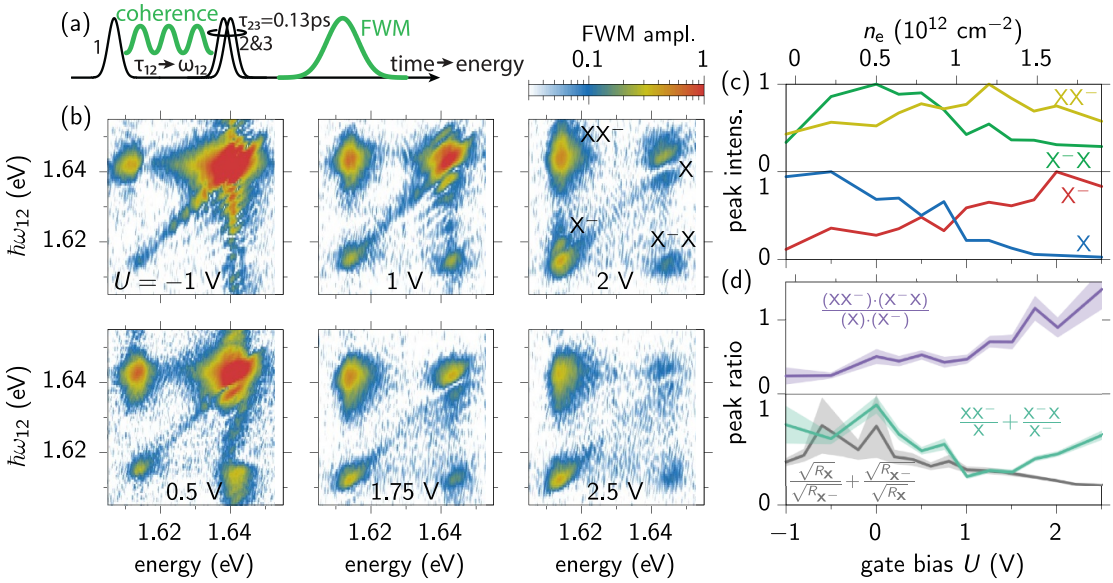

Figure 5. Phase-referenced two-dimensional FWM spectroscopy of X and X$^-$. (a) The pulse sequence used in the 2D FWM experiment. τ_{12} is scanned, while the other delay is set to $\tau_{23} = 0.13$ ps maximizing the coherent coupling. (b) Examples of 2D FWM spectra for different gate biases as given in the plots. (c) Integrated peak amplitudes of the four peak X, X, XX$^-$, and X$^-$X (marked in (b)) as function of gate bias. (d) Characteristic peak rations extracted from (c) as dots and from figure 1(c) as gray line. The shaded areas in (c) and (d) mark the uncertainty ranges.

the interplay between X and X$^-$ and reveal their coupling, we excite them in tandem, as shown spectrally in figure 4(a) by the laser spectrum in red and the FWM spectrum in blue. The measured spectrally resolved population dynamics are presented in (b). Interestingly, for the initial delays $\tau_{23} < 0.5$ ps, the FWM displays a beating particularly pronounced on the X$^-$ resonances. The first driving beam induces the Raman coherence between X and X$^-$ as depicted schematically in (b). Due to the spectral splitting δ between X and X$^-$, the density grating generated by the second beam oscillates with the period $2\pi\hbar/\delta \approx 0.14$ ps. The FWM released by the probe therefore shows the Raman quantum beat [57], as confirmed by the simulation in (c), and directly shown in (d) as time traces after spectrally integrating over the X$^-$ peak. This result indicates that X and X$^-$ are Raman-coupled, as they share a common ground state. Note, that the simulation (pale green line) only considers a single exciton decay channel, while in the experiment (green dots) the interplay between different relaxation paths leads to the rising signal for $\tau_{23} > 0.5$ ps (see figure 3).

A beating of a similar origin is observed in the coherence dynamics, probed by the τ_{12}-dependence, as shown in SI figure S6. When coherently coupled, the first-order absorptions of X and X$^-$, created by the leading pulse, are mutually converted into the FWM of X$^-$ and X, respectively, by the following two pulses, as schematically shown in figure 5(a). To pinpoint this phenomenon we perform two-dimensional (2D) FWM spectroscopy [58, 59]. In this approach,

originating from nuclear magnetic resonance spectroscopy, Fourier transformations are performed along two time axes: the direct time axis and the indirect delay axis [60–62]. In our case, the transform along the direct axis is automatically performed by the optical spectrometer, yielding the FWM spectra. Conversely, the Fourier transform of the indirect axis has to be recovered from the τ_{12}-sequence. To track the FWM phase when varying τ_{12}, we apply the phase-referencing scheme [63], which overcomes the need for an active phase-stabilization and permits us to accurately perform the Fourier transform along τ_{12}, yielding the energy axis $\hbar\omega_{12}$.

A conclusive display for the coherent coupling between X and X^- is presented in figure 5(b), showing 2D FWM amplitude spectra for selected gate voltages as labeled in the pots. The delay between pulses 2 and 3 was chosen to $\tau_{23} = 0.13$ ps, which locates us in the coherent coupling range as demonstrated in the SI figure S7. We have checked that for $\tau_{23} > 1$ ps the X and X^- coupling is present (see figure S8), although dominated by an incoherent population transfer between the two complexes [26]. Conceptually, the 2D FWM spectra of our V-shaped system consist of only four peaks. For the diagonal pair, labeled X^- and X, detection energy and $\hbar\omega_{12}$ energy are identical: FWM emission arises from the same absorption. Decisively, we clearly detect off-diagonals, labeled XX^- and X^-X. This means that the FWM of the charged exciton is also driven by the neutral exciton's first-order absorption, and vice-versa, respectively. Such coherent coupling was previously reported in semiconductor nanostructures [48, 59, 64], including TMDs [28, 59, 65]. Here, thanks to the tunability of n_e in this gated $MoSe_2$, we obviously find that the coherent nonlinear optical response of the $X-X^-$ complex can be controlled simply by applying an external bias.

The variation of the peak amplitudes in the 2D spectra with changing gate bias has two potential reasons: (i) change of the dipole strengths of X and X^- due to additional free charges, as already demonstrated in the reflectivity measurement in figure 1(b), (ii) the coherence transfer between both exciton species is affected by the free carriers. To disentangle these two effects we need to quantify the strength of the coherent coupling depending on n_e. In panel (c) we plot the peaks' integrated amplitudes versus the gate bias, where we expectedly find that X (blue) clearly drops, while X^- (red) builds up when increasing the carrier density. At the same time the off-diagonal peaks (green and yellow)—representing the coupling—show no clear trend. As mentioned before, the variation of the reflectivity spectrum upon an applied gate bias indicates a change of the dipole strengths of X and X^- and therefore of the pulse areas θ_X and θ_{X^-} applied to the two transitions. Note, that we do not consider any specific origin for the change of the strength of optical response of X and X^-. Now, in order to extract the strength of the $X-X^-$ coupling found in the 2D spectra, we can extract a quantity that does not depend on the pulse areas. To achieve this, we note that the amplitudes of diagonal peaks scale as θ_X^3 and $\theta_{X^-}^3$, whereas the off-diagonals follow the scaling $\theta_X^2\theta_{X^-}$ for XX^- and $\theta_X\theta_{X^-}^2$ for X^-X. Plotting now the expression, $XX^-\cdot X^-X/(X\cdot X^-)$ in figure 5(d, top) the pulse areas and therefore the dipole strengths cancel out. We see though, that this quantity increases with the electron density, indicating the increase of the coupling strength.

Another insightful quantity that can be extracted from the reflectivity spectra and the 2D spectra is the sum of peak ratios. For the 2D spectra we calculate $XX^-/X+X^-X/X^-$, which translates into pulse areas as $\theta_{X^-}/\theta_X + \theta_X/\theta_{X^-}$. To extract an equivalent quantity from the reflectivity spectra we need to calculate $\sqrt{R_{X^-}}/\sqrt{R_X} + \sqrt{R_X}/\sqrt{R_{X^-}}$ from the peak intensities R_X and R_{X^-}. The two quantities are plotted (normalized to unity) in figure 5(d) as turquoise dots for 2D and gray line for reflectivity. The behavior of both curves is rather unspecific for negative and small gate voltages, where X^- is only weakly addressed if present at all. Note, that in this range of bias values the X^- is very weak which is leading to the relatively large uncertainties (shaded areas). Therefore, the peak ratios in this range are not particularly significant and we do not expect to draw conclusions from this bias range. However, the 2D spectra result shows a clearly growing trend for increasing charge densities, while the reflectivity results shrink. This discrepancy is a second hint that the variation of the dipole strengths with increasing gate bias alone, cannot fully explain the variation of the coherent coupling between X and X^- observed in 2D FWM.

6. Conclusions and outlook

FWM spectroscopy methods are powerful tools that have led in the recent years to a significant improvement of the understanding of the rich exciton physics in TMDs. This has established the method as a versatile technique for studies of atomically thin materials and TMD-based heterostructures as detailed in the Introduction. However, so far a particular focus on the important issue of the free carrier influence on the studied phenomena has been missing. A factor that fundamentally affects the optical response of TMDs, and governs even the most basic characteristics like the number and respective intensities of different exciton states.

Using FWM micro-spectroscopy, we have shown that the homogeneous linewidth and population lifetime of excitonic complexes hosted by a $MoSe_2$-monolayer-based van der Waals heterostructure can be tuned via the free electron density, which is injected by a gate bias applied to our device. With increasing gate bias, the exciton's inhomogeneous broadening decreases, reflecting the screening of the

disorder via free the electron gas, which also increases the excitons' radiative decay rates. Conversely, the homogeneous broadening increases, which is attributed to the combined increase of the radiative decay rate and the conversion rate of the neutral exciton towards the charged one. By exciting the neutral (X) and charged exciton (X^-) simultaneously and probing the population dynamics we demonstrated that the coherence between X and X^- leads to a characteristic quantum beat in the FWM signal. By then performing 2D FWM spectroscopy for a variety of applied gate biases, we have further demonstrated that the $X-X^-$ coherent coupling can be controlled by the gate voltage, and hence by the free electron density. Through considering specific peak ratios, we were able to demonstrate that the change of coherent coupling can be disentangled from the variation of dipole strengths arising from the injection of free carries. An increase of the coupling strength with n_e could be linked with the screening of disorder via the electron gas. This illustrates the utility and versatility of ultrafast nonlinear spectroscopy in investigating optical responses of excitonic systems, going beyond the capabilities of linear methods.

In future developments, by performing FWM with spatially separated driving beams, while using devices hosting highly diffusive excitons, it will be possible to achieve non-local coherent coupling in a 2D semiconductor. Combining this approach with two-color FWM spectroscopy would also permit to selectively address the coherence transfer between neutral and charged excitons. Our findings yield exciting prospects for forthcoming investigations of coherent phenomena in the context of recent discoveries of strongly-correlated exciton phases in solids [31], optically probed quantum Hall states [32], moiré superlattices [66], and magnetic 2D materials [67]. In practice, coherent nonlinear spectroscopy could be used to optically infer the dephasing processes of the Umklapp branches of TMD Wigner crystals and fractional quantum Hall states in graphene.

Data availability statement

The data that support the findings of this study are available upon reasonable request from the authors.

Acknowledgments

This work was supported by the Polish National Science Centre under decisions DEC-2020/39/B/ST3/03251. The Warsaw team (A R, P K and M P) acknowledges support from the ATOMOPTO project (TEAM program of the Foundation for Polish Science, co-financed by the EU within the ERDFund), CNRS via IRP 2D Materials, EU Graphene Flagship. M P acknowledges support by the Foundation for Polish Science (MAB/2018/9 Grant within the IRA Program financed by EU within SG OP Program). The Polish participation in the European Magnetic Field Laboratory (EMFL) is supported by the DIR/WK/2018/07 of MEiN of Poland. A R acknowledges support of this work from the Diamentowy Grant under decision DI2017008347 of MEiN of Poland. K W and T T acknowledge support from the Elemental Strategy Initiative conducted by the MEXT, Japan, (Grant No. JPMXP0112101001), JSPS KAKENHI (Grant No. JP20H00354), and the CREST (JPMJCR15F3), JST. J H acknowledges support from EPSRC doctoral prize fellowship. D W was supported by the Science Foundation Ireland (SFI) under Grant 18/RP/6236. We thank Ronald Cox and Julien Renard for their constructive comments on the manuscript, Rafał Bożek for the AFM measurement of the hBN thicknesses, and Tilmann Kuhn for helpful discussions.

ORCID iDs

Aleksander Rodek https://orcid.org/0000-0002-0263-3122
James Howarth https://orcid.org/0000-0001-7434-9940
Kenji Watanabe https://orcid.org/0000-0003-3701-8119
Piotr Kossacki https://orcid.org/0000-0002-7558-1044
Jacek Kasprzak https://orcid.org/0000-0003-4960-2603

References

[1] Splendiani A, Sun L, Zhang Y, Li T, Kim J, Chim C-Y, Galli G and Wang F 2010 *Nano Lett.* **10** 1271–5
[2] Mak K F, Lee C, Hone J, Shan J and Heinz T F 2010 *Phys. Rev. Lett.* **105** 136805
[3] Raja A *et al* 2017 *Nat. Commun.* **8** 15251
[4] Van Tuan D, Yang M and Dery H 2018 *Phys. Rev.* B **98** 125308
[5] Chernikov A, Berkelbach T C, Hill H M, Rigosi A, Li Y, Aslan O B, Reichman D R, Hybertsen M S and Heinz T F 2014 *Phys. Rev. Lett.* **113** 076802
[6] Wang G, Chernikov A, Glazov M M, Heinz T F, Marie X, Amand T and Urbaszek B 2018 *Rev. Mod. Phys.* **90** 021001
[7] Stepanov P *et al* 2021 *Phys. Rev. Lett.* **126** 167401
[8] Geim A K and Grigorieva I V 2013 *Nature* **499** 419–25
[9] Cadiz F *et al* 2017 *Phys. Rev.* X **7** 021026
[10] Mak K F, He K, Shan J and Heinz T F 2012 *Nat. Nanotechnol.* **7** 494–8
[11] Zeng H, Dai J, Yao W, Xiao D and Cui X 2012 *Nat. Nanotechnol.* **7** 490–3
[12] Mak K F, McGill K L, Park J and McEuen P L 2014 *Science* **344** 1489–92
[13] Kioseoglou G, Hanbicki A T, Currie M, Friedman A L, Gunlycke D and Jonker B T 2012 *Appl. Phys. Lett.* **101** 221907
[14] Cao T *et al* 2012 *Nat. Commun.* **3** 887
[15] Wierzbowski J *et al* 2017 *Sci. Rep.* **7** 12383
[16] Ajayi O A *et al* 2017 *2D Mater.* **4** 031011
[17] Manca M *et al* 2017 *Nat. Commun.* **8** 14927
[18] Lindlau J *et al* 2018 *Nat. Commun.* **9** 2586
[19] Jakubczyk T *et al* 2019 *ACS Nano* **13** 3500–11
[20] Boule C, Vaclavkova D, Bartos M, Nogajewski K, Zdražil L, Taniguchi T, Watanabe K, Potemski M and Kasprzak J 2020 *Phys. Rev. Mater.* **4** 034001
[21] Hahn T *et al* 2022 *Adv. Sci.* **9** 2103813

[22] Jakubczyk T, Delmonte V, Koperski M, Nogajewski K, Faugeras C, Langbein W, Potemski M and Kasprzak J 2016 *Nano Lett.* **16** 5333–9
[23] Jakubczyk T, Nogajewski K, Molas M R, Bartos M, Langbein W, Potemski M and Kasprzak J 2018 *2D Mater.* **5** 031007
[24] Hao K *et al* 2016 *Nat. Phys.* **12** 677–82
[25] Hao K *et al* 2017 *2D Mater.* **4** 025105
[26] Moody G *et al* 2015 *Nat. Commun.* **6** 8315
[27] Conway M, Muir J, Earl S, Wurdack M, Mishra R, Tollerud J and Davis J 2022 *2D Mater.* **9** 021001
[28] Hao K *et al* 2017 *Nat. Commun.* **8** 15552
[29] Ross J S *et al* 2013 *Nat. Commun.* **4** 1474
[30] Jones A M *et al* 2013 *Nat. Nanotechnol.* **8** 634–8
[31] Smoleński T *et al* 2021 *Nature* **595** 53–57
[32] Popert A, Shimazaki Y, Kroner M, Watanabe K, Taniguchi T, Imamoğlu A and Smoleński T 2022 *Nano Lett.* **22** 7363–9
[33] Efimkin D K and MacDonald A H 2017 *Phys. Rev.* B **95** 035417
[34] Chang Y-W and Reichman D R 2019 *Phys. Rev.* B **99** 125421
[35] Kossacki P, Cibert J, Ferrand D, Merle d'Aubigné Y, Arnoult A, Wasiela A, Tatarenko S and Gaj J A 1999 *Phys. Rev.* B **60** 16018–26
[36] Kossacki P, Pochocka P, Piechal B, Maślana W, Golnik A, Cibert J, Tatarenko S and Gaj J A 2005 *Phys. Rev.* B **72** 035340
[37] Hawrylak P 1991 *Phys. Rev.* B **44** 3821–8
[38] Brinkmann D, Kudrna J, Gilliot P, Hönerlage B, Arnoult A, Cibert J and Tatarenko S 1999 *Phys. Rev.* B **60** 4474–7
[39] Koch M, Hellmann R, Bastian G, Feldmann J, Göbel E O and Dawson P 1995 *Phys. Rev.* B **51** 13887–90
[40] Schultheis L, Kuhl J, Honold A and Tu C W 1986 *Phys. Rev. Lett.* **57** 1797–800
[41] Wang H, Ferrio K, Steel D G, Hu Y Z, Binder R and Koch S W 1993 *Phys. Rev. Lett.* **71** 1261–4
[42] Wegener M, Chemla D S, Schmitt-Rink S and Schäfer W 1990 *Phys. Rev.* A **42** 5675–83
[43] Rodek A *et al* 2021 *Nanophotonics* **10** 2717–28
[44] Akbari H, Biswas S, Jha P K, Wong J, Vest B and Atwater H A 2022 *Nano Lett.* **22** 7798–803
[45] Savona V and Langbein W 2006 *Phys. Rev.* B **74** 075311
[46] Rossi F and Kuhn T 2002 *Rev. Mod. Phys.* **74** 895–950
[47] Shah J 1999 *Ultrafast Spectroscopy of Semiconductors and Semiconductor Nanostructures* (Heidelberg: Springer)
[48] Langbein W and Patton B 2006 *Opt. Lett.* **31** 1151–3
[49] Niehues I *et al* 2018 *Nano Lett.* **18** 1751–7
[50] Khatibi Z, Feierabend M, Selig M, Brem S, Linderälv C, Erhart P and Malic E 2018 *2D Mater.* **6** 015015
[51] Raja A *et al* 2019 *Nat. Nanotechnol.* **14** 832–7
[52] Christiansen D *et al* 2017 *Phys. Rev. Lett.* **119** 187402
[53] Scarpelli L, Masia F, Alexeev E M, Withers F, Tartakovskii A I, Novoselov K S and Langbein W 2017 *Phys. Rev.* B **96** 045407
[54] Zipfel J, Wagner K, Semina M A, Ziegler J D, Taniguchi T, Watanabe K, Glazov M M and Chernikov A 2022 *Phys. Rev.* B **105** 075311
[55] Ciulin V, Kossacki P, Haacke S, Ganiére J-D, Deveaud B, Esser A, Kutrowski M and Wojtowicz T 2000 *Phys. Rev.* B **62** R16310
[56] Kossacki P 2003 *J. Phys.: Condens. Matter* **15** R471
[57] Mermillod Q *et al* 2016 *Optica* **3** 377–84
[58] Li X, Zhang T, Borca C N and Cundiff S T 2006 *Phys. Rev. Lett.* **96** 057406
[59] Singh A, Moody G, Wu S, Wu Y, Ghimire N J, Yan J, Mandrus D G, Xu X and Li X 2014 *Phys. Rev. Lett.* **112** 216804
[60] Hamm P and Zanni M 2011 Basics of 2D IR spectroscopy *Concepts and Methods of 2D Infrared Spectroscopy* (Cambridge: Cambridge University Press) pp 61–87
[61] Moody G and Cundiff S T 2017 *Adv. Phys.* X **2** 641–74
[62] Smallwood C L and Cundiff S T 2018 *Laser Photonics Rev.* **12** 1800171
[63] Delmonte V, Specht J F, Jakubczyk T, Höfling S, Kamp M, Schneider C, Langbein W, Nogues G, Richter M and Kasprzak J 2017 *Phys. Rev.* B **96** 041124
[64] Kasprzak J, Patton B, Savona V and Langbein W 2011 *Nat. Photon.* **5** 57–63
[65] Hao K, Xu L, Nagler P, Singh A, Tran K, Dass C K, Schüller C, Korn T, Li X and Moody G 2016 *Nano Lett.* **16** 5109–13
[66] Tran K *et al* 2019 *Nature* **567** 71–75
[67] Wilson N P *et al* 2021 *Nat. Mater.* **20** 1657–62